Follow the Trace: Becoming a Seismo-Detective with a Campus-Based Raspberry Shake Seismometer

Eric Löberich*1[®] and Maureen D. Long¹

Abstract

Seismic signals, whether caused by earthquakes, other natural phenomena, or artificial noise sources, have specific characteristics in the time and frequency domains that contain crucial information reflecting their source. The analysis of seismic time series is an essential part of every seismology-oriented study program. Enabling students to work with data collected from their own campus, including signals from both anthropogenic and natural seismic sources, can provide vivid, practical examples to make abstract concepts communicated in classes more concrete and relevant. Data from research-grade broadband seismometers enable us to record time series of vibrations at a broad range of frequencies; however, these sensors are costly and are often deployed in remote places. Participation in the Raspberry Shake citizen science network enables seismology educators to record seismic signals on our own campuses and use these recordings in our classrooms and for public outreach. Yale University installed a Raspberry Shake three-component, low-cost seismometer in the Earth and Planetary Sciences department building in Summer 2022, enabling the detection of local, regional, and teleseismic earthquakes, microseismic noise, and anthropogenic noise sources from building construction, an explosive event in a steam tunnel, and general building use. Here, we discuss and illustrate the use of data from our Raspberry Shake in outreach and education activities at Yale. In particular, we highlight a series of ObsPy-based exercises that will be used in courses taught in our department, including our upper-level Introduction to Seismology course and our undergraduate classes on Natural Disasters and Forensic Geoscience.

Cite this article as Löberich, E., and M. D. Long (2024). Follow the Trace: Becoming a Seismo-Detective with a Campus-Based Raspberry Shake Seismometer, *Seismol. Res. Lett.* **95**, 2538–2553, doi: 10.1785/0220230365.

Supplemental Material

Introduction

Earthquakes are one of the most fascinating and dangerous phenomena on our planet and are a focus of strong public fascination. Raising awareness of earthquake hazard, and illustrating the potential of seismic waves to improve our understanding of Earth's structure and dynamics, are of key importance for commonly taught Earth science classes. However, illustrating the concepts of seismology with vivid and relevant examples in a classroom setting can be challenging, given the spatially and temporally uneven distribution of earthquakes, the invisible nature of seismic wave propagation, and the lack of geographic proximity to earthquakes at many institutions.

A practical approach to enhance the relevance of seismology concepts is provided by the Raspberry Shake citizen science network. Raspberry Shakes are relatively low-cost and easy-to-install seismometers for which data can easily be viewed and shared via the Internet using tools such as the ShakeNet app. These devices are suitable for private households, citizen

scientists, and hobbyists, and are also appealing for classroom teaching and outreach purposes, as well as having applications in basic and applied research. Physical access to a seismometer, as well as opportunities to analyze and learn from data collected on one's own campus, have the potential to make teaching about seismology concepts more exciting and relevant for students. Similarly, the incorporation of locally collected data into public talks and outreach events can make earthquakes and their hazards more tangible for audiences. There are many successful examples of "Seismology in Schools" programs, including those that have used Raspberry Shake sensors (e.g., Diaz et al., 2020; Subedi et al., 2020). To explore the utility of an educational

^{1.} Earth and Planetary Sciences, Yale University, New Haven, Connecticut, U.S.A., https://orcid.org/0000-0002-4862-7457 (EL); https://orcid.org/0000-0003-1936-3840 (MDL)

^{*}Corresponding author: eric.loeberich@yale.edu

[©] Seismological Society of America

seismometer in a university setting, Yale's Earth and Planetary Sciences department installed a Raspberry Shake three-component sensor (RS3D) at the end of July 2022 and joined the Raspberry Shake seismic network.

Here, we share our experiences with the first year of data collected with Yale's Raspberry Shake and introduce ideas for classroom demonstrations and exercises using data from the instrument for use in Yale classes, including Natural Disasters, Forensic Geoscience, and Introduction to Seismology courses. Our sensor has effectively recorded dozens of regional and teleseismic earthquakes, as well as both natural and anthropogenic noise sources, allowing us to illustrate a range of fundamental concepts in observational seismology, seismotectonics, wave propagation, signal processing, and forensic seismology. We discuss a range of data products and material for classroom exercises, focusing on concepts such as data preprocessing, determination of sensor orientation, identification of different types of seismic waves, noise levels at different frequencies, characterization of natural (microseism) and anthropogenic noise, and investigation of a forensic event (a steam tunnel leak at an on-campus construction site).

Installing a Raspberry Shake Seismometer at Yale

The compact design and easy-to-install nature of low-cost Raspberry Shake devices opens a diverse field of possible applications. They have been used not only in the study of earthquakes (e.g., Calais et al., 2019) but also for recording elephants (Lamb et al., 2021) and monitoring rockfalls (Manconi et al., 2018) and icequakes (Winter et al., 2021) (see e.g., Raspberry Shake, 2023). Figure 1 shows photos of (Fig. 1a) our RS3D sensor (R3547) and (Fig. 1b) its installation configuration. The device itself is built upon a Linux-driven Raspberry Pi minicomputer connected to three orthogonally aligned 4.5 Hz geophones (with electronic longer-period extension to 2 s) that record ground vibrations along the north-south, east-west, and Z orientations (for more technical details see Raspberry Shake, 2018, 2020). These time series of velocities are digitized with a sampling rate of 100 samples per second, saved internally for seven days, and transferred via ethernet to a Raspberry Shake server that grants open data access (via programs such as Station View or Swarm) to all stations in the network. Figure 1c shows the "live-stream" feature of Station View as displayed on the rotating information screen in the lobby of the Kline Geology Laboratory (KGL) to inform visitors and colleagues in the Earth and Planetary Sciences Department about recent ground motion in our building. R3547 was installed in an enclosed room with a concrete floor in the subbasement of KGL (b), leading us to expect good ground coupling and minimal instrument tilt. The sensor was leveled based on the internal bubble level and oriented using a compass at the time of installation. However, given the difficulty of relying on a compass inside a building, we later checked the alignment using the measured polarization of P waves, as described subsequently.

Earthquake Recordings

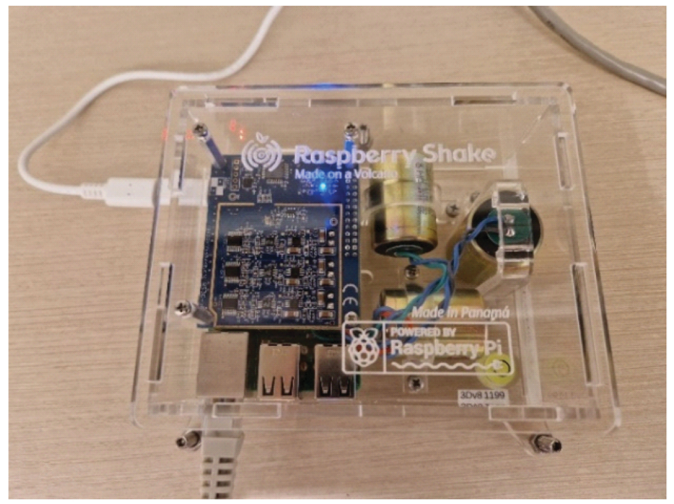
Exercise 1: detecting and characterizing signals from notable earthquakes

During the first year of recording, we observed (\hat{=} with relatively clear phase onset) approximately five dozen significant earthquakes from different source regions (local to teleseismic). To illustrate how our Raspberry Shake recordings can be used to teach about earthquakes, we focus on the areas of North, Central, and northern South America with a particularly high number of observed events that provide records suitable to be analyzed during a classroom exercise. However, the parameters for this exercise can easily be adjusted by the instructor to, for example, look at waveforms for all earthquakes above a certain magnitude in a given earthquake catalog. Figure 2a shows the locations of 28 earthquakes that were detected in our selected regions between 19 September 2022 and 19 July 2023. Those events contained in the Global Centroid Moment Tensor (Global CMT) catalog (Dziewonski et al., 1981; Ekström et al., 2012; see Data and Resources) are plotted with their focal mechanism solutions; other events are shown with a star. Location parameters for the latter events were retrieved from the Earthscope (Incorporated Research Institutions for Seismology) client implemented in ObsPy (Beyreuther et al., 2010; Megies et al., 2011; Krischer et al., 2015), a Python library that facilitates handling seismic data (see Data and Resources).

Most of the earthquakes are shallow events (<30 km), but deeper earthquakes were observed as well. We recorded a magnitude $M_{\rm w}$ 6.7 event at ~65 km depth near the coast of Ecuador, an $M_{\rm w}$ 5.3 and an $M_{\rm w}$ 5.4 beneath northern Columbia at depths of ~158 km and ~160 km, respectively, an $M_{\rm w}$ 6.2 at ~164 km depth beneath the Leeward Islands, and an $M_{\rm w}$ 6.4 event beneath Guatemala at a depth of ~253 km. As expected, the distribution of earthquakes correlates well with the locations of plate boundaries (e.g., Bird, 2003). We detected waves associated with mostly strike-slip earthquakes on the west coast of North America, reverse faulting in the Cocos and Mexico subduction zones, and normal faulting in western Texas. Despite the relatively short observation time, and the fact that Yale is located far away from plate boundaries, we did detect a few moderately strong local to regional events, including an $m_{\rm bLg}$ 3.3 in Maine, two earthquakes with $M_{\rm wr}$ 3.6 and $m_{\rm bLg}$ 3.8 in New York State, and a somewhat stronger regional earthquake (m_b 4.5) offshore of the U.S. East Coast.

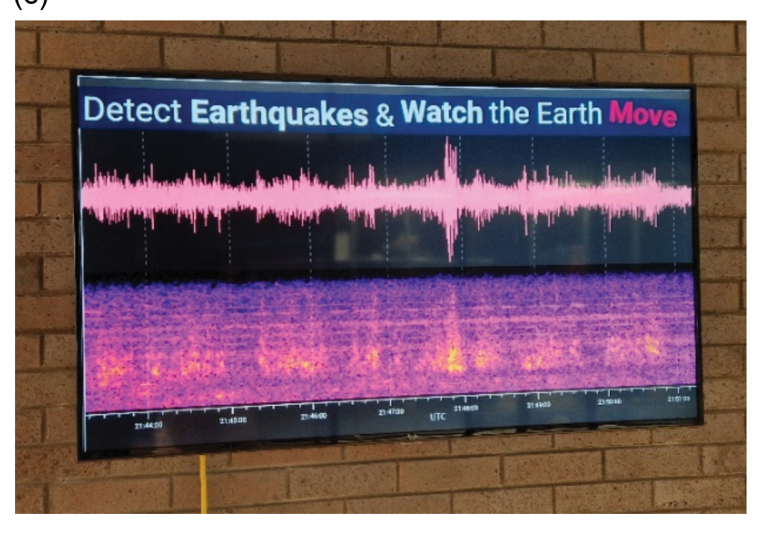
The maps shown in Figure 2a,b, along with Raspberry Shake records from two events (Fig. 2c), can be used to illustrate several fundamental concepts in seismology and earthquake hazards. These include the preferential location of earthquakes along plate boundaries, the existence of intraplate earthquakes, the type of faulting that controls the earthquake mechanisms, the types of waves that are generated by earthquakes and how they can be identified on seismograms, and the concepts of

(a) (b)





(c)



aftershocks, earthquake magnitudes, and ground-motion amplitudes.

Figure 2c shows seismograms for the $M_{\rm w}$ 7.7 earthquake in Michoacan, Mexico, on 19 September 2022, which was the largest event recorded during our observation period in this study area, along with an $M_{\rm w}$ 6.7 aftershock that occurred three days later, on 22 September. Figure 2b shows focal mechanisms for both events superimposed on the slab depth contours of the Slab2 model (Hayes *et al.*, 2018). Preprocessed and filtered Raspberry Shake records indicate clear body- and surface-wave arrivals for mainshock and aftershock on all three components. Given the similar origin and source mechanism of both events, it is not surprising that phase arrivals are well correlated. However, due to the lower magnitude, the amplitudes of the aftershock waves are significantly smaller, providing a clear illustration of how the amplitude of ground motion depends on the size of the earthquake.

We envision using the maps and seismograms shown in Figure 2 to illustrate basic concepts related to earthquakes and seismic waves in Yale's introductory Natural Disasters

Figure 1. Photos of the Yale Raspberry Shake (R3547) installation. (a) The RS3D sensor is built upon a Raspberry Pi computer (visible at left) that is connected to power and ethernet, with attached geophones of different alignment (north–south, east–west, Z, visible at right). (b) R3547 installed on the concrete floor in the sub-basement of the Kline Geology Laboratory (KGL). (c) Unfiltered "live-stream" in (top) time and (bottom) frequency domains embedded from the Raspberry Shake Station View, displayed on the rotating informational screen in the lobby of KGL.

class, which includes units on earthquakes and plate tectonics. Students in more advanced classes, such as Introduction to Seismology, can be asked to download and preprocess Raspberry Shake records for notable earthquakes that occur during the semester, to identify and characterize the seismic phases that appear on the seismograms, and to explain how the tectonic settings in terms of the focal mechanisms might control the amplitudes of different waves.

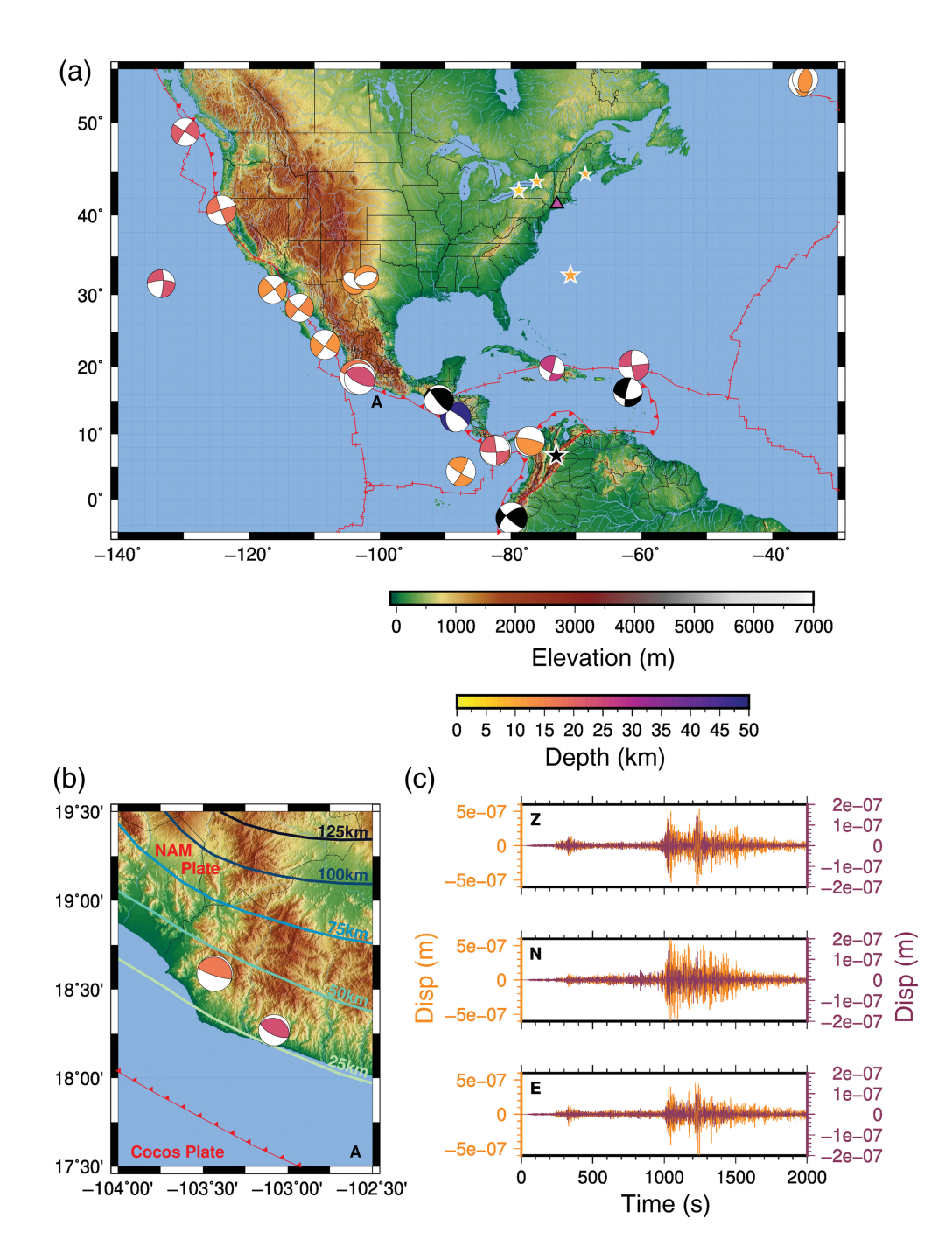
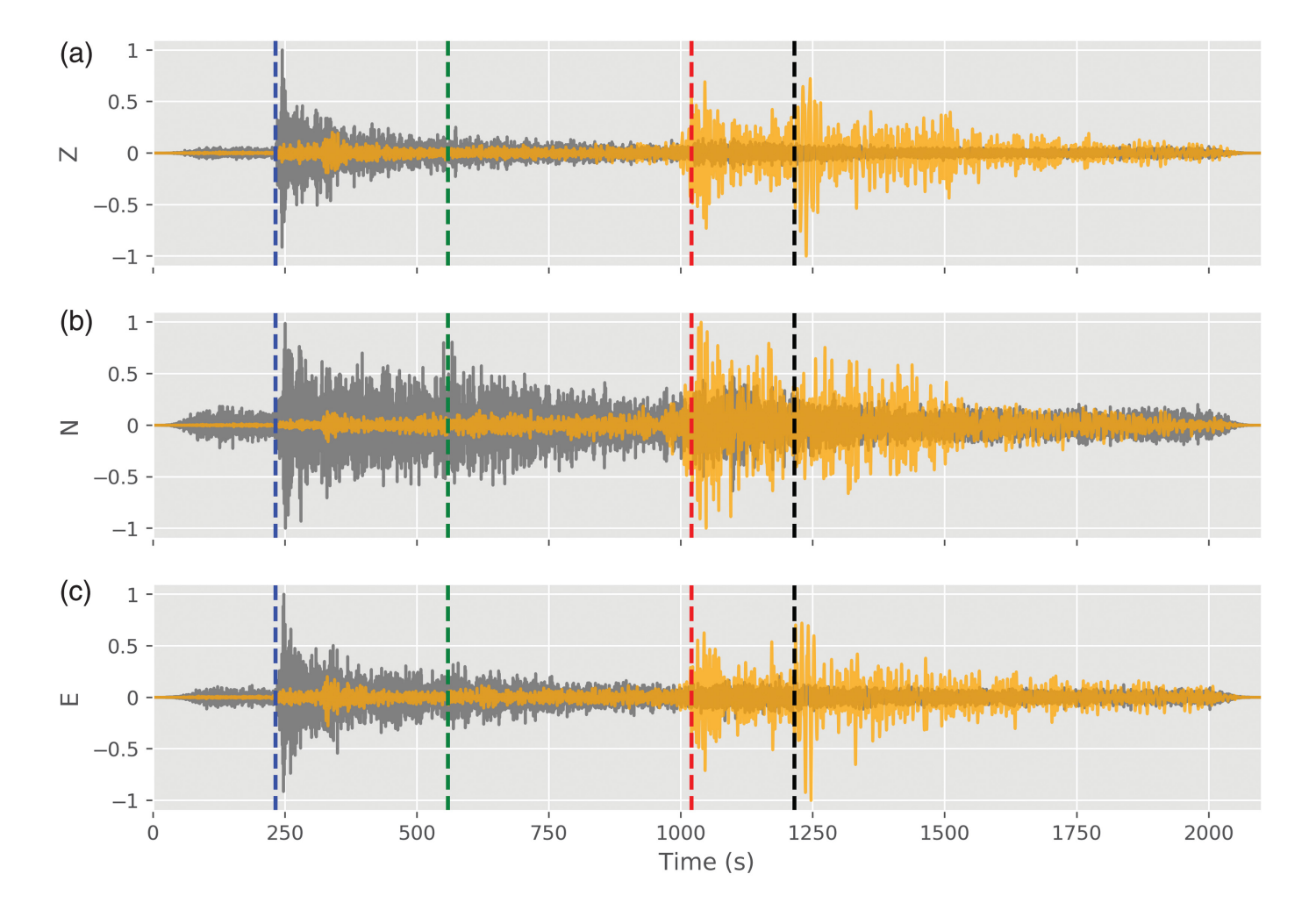


Figure 2. Overview on earthquakes recorded by the Yale Raspberry Shake (R3547) between 19 September 2022 and 19 July 2023. (a) Map of events in and around North, Central, and northern South America detected by R3547 (magenta triangle). Earthquakes are shown with focal mechanism plots as defined by their centroid moment tensor (CMT); size scales with magnitude, and color represents depth (see scale bar; black: >50 km). Events without CMT solutions are shown by a star. Plate boundaries of Bird (2003) are overlain on topography from ETOPO1 (colored according to scale bar). (b) Zoom on Mexico's Pacific coast showing the locations of an $M_{\rm w}$ 7.7 mainshock and its $M_{\rm w}$ 6.7 aftershock within the Cocos subduction zone. Slab-depth contours are taken from the Slab2 model (Hayes *et al.*, 2018) shown on high-resolution topography (all Generic Mapping Tools [GMT] map data sets are referenced in Data and Resources). (c) R3547 time series of displacements (Disp; 1e-07 = 1 × 10⁻⁷) for each component (after preprocessing and filtering), indicating similar body- and surface-wave phase arrivals for the mainshock (orange) and aftershock (maroon). The vertical scale for each earthquake is represented by the respective *y* axis (as indicated by colors) and differs between the two events.

Exercise 2: signal preprocessing techniques and application to earthquake records

The preprocessing of data before analysis is an important part of observational seismology and is a topic covered in several of Yale's seismology courses, Introduction including Seismology. Here, we develop a classroom exercise based on standard ObsPy routines to enhance the quality of our time series before formal analysis and remove the instrument response. We follow examples of Raspberry Shake's Developer's corner, the ObsPy tutorial, Seismo-Live Computational Seismology (see Data and Resources) to build a Jupyter Notebook (similar for the other exercises) that can be shared with students to detrend, demean, taper, and deconvolve (including prefilter and water level, see supplemental exercise 2.1, available in the supplemental material to this article, and Data and Resources) seismic records.

We next experiment with filter parameters to best identify different phase arrivals. Here, we consider a set of distance-dependent band-pass filters that do not introduce a phase shift (so-called zerophase shift; see Data and Resources). Two of them focus on comparably higher frequencies (hfbf) and another one on lower frequencies (lfbf). For events at a hypocentral distance $<10^{\circ}$ (1° \cong 111 km, so less than ~1200 km), hfbf is set to 1.3-4 Hz. Local seismicity is often analyzed at even higher frequencies (up to 15 Hz); however, based on the distribution of spectral energy



observed for our examples, this does not appear necessary for our later investigation. The filter can be adjusted easily during classroom exercises if required (see NY State $M_{\rm wr}$ 3.6 in supplemental exercise 2.2). At larger distances, hfbf targets a frequency range between 0.7 and 2 Hz. For these distances, we further define the lfbf considering 0.05–0.7 Hz (for a discussion of the resolution of even lower frequencies see supplemental exercise 2.3). After filtering, we decimate the sampling rate from 100 samples per second to df = 33.3 Hz, which enhances computational efficiency and, given the Nyquist frequency, is still sufficient to sample the filtered range appropriately.

Figure 3 shows overlays of lfbf- and hfbf-filtered time series for the same $M_{\rm w}$ 7.7 Mexico earthquake (at an epicentral distance of 34°). To identify phase onsets, we calculate expected arrival times of P and S wave based on ray theory for the IASP91 velocity model (Kennett and Engdahl, 1991) with ObsPy. The P-wave onset dominates the hfbf traces (0.7–2 Hz); however, the S-wave arrival is barely visible in the P-wave coda. Another onset between P and S, visible on the lfbf records (0.05–0.7 Hz), is related to the arrival of the PP phase. In contrast to the body waves, which are well elucidated by the hfbf scheme, the lfbf band reveals striking surface-wave arrivals. We estimated the propagation velocities needed to match the arrival times of the two dominant phase arrivals

Figure 3. Preprocessed, band-pass filtered (gray: 0.7–2 Hz; orange: 0.05–0.7 Hz), and normalized (scaled by the absolute maximum per component on each trace) records of the $M_{\rm w}$ 7.7 Mexico mainshock for each of the three components (a) Z, (b) N, and (c) E; dashed vertical lines show expected phase arrival times (blue: P; green: S; red: Love [$\overline{\nu_{\rm Lg}} = 3.2 \ {\rm km/s}$]; black: Rayleigh [$\overline{\nu_{\rm Rg}} = 2.75 \ {\rm km/s}$]).

on the Z and E components and found average velocities of \sim 3.2 km/s for Love waves and \sim 2.75 km/s for Rayleigh waves (for further reading on frequency dependence, see e.g., Ekström, 2014).

In the context of a classroom exercise for Introduction to Seismology, students will be asked to preprocess the data for this particular earthquake, apply a range of filters and explain what they see at different frequencies, identify different phase arrivals and explain their reasoning, and estimate average Love and Rayleigh wave propagation velocities along the Mexico–New Haven path.

Exercise 3: determination and correction of sensor misorientation

Determining the orientation of a seismic sensor is important in several applications, including for ocean-bottom seismometer (OBS) data for which the sensor orientation is completely unknown (e.g., Lynner et al., 2019) or for cases in which a sensor was accidentally misoriented upon installation. Correct sensor orientation is particularly crucial in applications that rely on estimates of seismic-wave polarization, such as shear-wave splitting observations (e.g., Hanna and Long, 2012; Reiss et al., 2019). Proper orientation of a seismic instrument is particularly challenging for indoor installations because the presence of metal in buildings can interfere with the use of a compass. Here, we suggest a classroom exercise for Introduction to Seismology to determine and correct for the possible misorientation of our Raspberry Shake sensor during installation.

To do this, we take advantage of the characteristics of the Pwave phase, which should be polarized toward the direction of the earthquake origin (see e.g., Zenhäusern et al., 2022). We consider a single event for our analysis, a deep (z = 253 km) M_w 6.4 earthquake in Guatemala. Because of its hypocentral depth, the arrivals are undisturbed by complex surface structures near the source side and its records are exceptionally clear. Estimating the misorientation requires a determination of the difference between the observed P-wave polarization and the actual station-to-event azimuth (the back azimuth). Here, we follow one of the methods explained by Zenhäusern et al. (2022) to compute the apparent back azimuth, searching for the angle that, upon rotation toward the radial (R-) component, will maximize observed P-wave energy. Because this approach depends on the window length and frequencies used, we determine an initial set of possible solutions based on a range of parameters and evaluate them by a quality factor q_f (see supplemental exercise 3). Based on the difference between the apparent back azimuth of highest quality (211.73°) and the actual back azimuth (215.94°) for the Guatemala event, we estimate a sensor misorientation of only -4.21°, meaning that the sensor was nearly correctly oriented upon installation. In our subsequent analyses of Yale Raspberry Shake data, we apply a correction for this minor misorientation.

This classroom exercise will allow seismology students to understand and apply the concepts of wave polarization when they rotate seismometer components to the radial and transverse coordinate system. It will also allow them to apply mathematical concepts such as the short-term average/long-term average (STA/LTA), the average of the signal over short versus long time periods, or cross correlation in seismology, taking advantage of the practical implementation of data processing analysis in the ObsPy framework. Although this exercise was designed to be applied to data from our local Raspberry Shake instrument, it could be extended to OBS data or to other applications, and to different phases such as Rayleigh waves.

Exercise 4: investigation of regional earthquake phases

After introducing the tools required for preprocessing and sensor alignment correction, our next Introduction to Seismology

classroom exercise focuses on specific earthquakes in the northeastern United States, with the goal of familiarizing students with the characteristics of local to regional earthquake records. We observed three moderate earthquakes in our own "backyard" during the first year of recording (Fig. 2), two of them in New York and one in Maine. Because of the small epicentral distances (<5°) and the generally low attenuation in eastern North America (e.g., Zhao and Mousavi, 2018), the hfbf configuration (1.3–4 Hz) is most appropriate to emphasize the phase arrivals for all three events. We rotate the records into the ZRT coordinate system, accounting for the back azimuth and the small misorientation of the sensor. Figure 4 shows these records for each event, zoomed in to the maximum amplitude (the S-Lg package). Because of the events' proximity, S and surface waves arrive at similar times, and distinguishing them is difficult. Although the waveforms for both New York events (Fig. 4b,c) show similar tendencies, phase characteristics of the Maine earthquake (Fig. 4a) differ. The Maine event indicates more relative displacement on the Z component and comparably little on the T component. Moreover, the coincidence of phase energy on the R and Z components is indicative of an SV wave (e.g., Bormann et al., 2014). In terms of polarization, the particle motion in the horizontal plane (Fig. 4d) aligns more with the R component, and forms horizontally elongated ellipses in the R-Z plane (Fig. 4g), whereas the displacement in the T-Z plane is smaller and rather diffuse (Fig. 4j). For the New York earthquakes, energy on the T component might suggest the arrival of an SH wave (e.g., Bormann et al., 2014). Although the relative distribution of phase energy for the New York events looks similar, the onset appears more impulsive for the $m_{\rm bLg}$ 3.8 case (Fig. 4b) than for the $M_{\rm wr}$ 3.6 earthquake (Fig. 4c). For both events, we observe tendencies of elliptical particle motion of changing orientation in the horizontal plane (Fig. 4e,f); the polarization in the R-Z and T-Z plane (Fig. 4h,i and Fig. 4k,l) rather extends along the horizontal component. We envision a classroom exercise in which students are asked to identify the main phase arrivals, describe their polarizations, discuss the similarities and differences among the waveforms for the different events, and compare the characteristics of local and teleseismic earthquake recordings.

Noise Analysis and Anthropogenic Signals

In addition to records from earthquakes, the Yale Raspberry Shake continuously observes ambient noise. An overview of the diverse natural and anthropogenic sources that might have been recorded is provided by McNamara and Buland (2004) (see also McNamara and Boaz, 2019). Examples include ocean waves that couple with the ocean bottom at the shoreline, generating microseism, wind gusts that sway buildings, heavy machinery (e.g., wind turbines, oil pumps, heating and ventilation systems, and synchronous machines), traffic (e.g., cars,

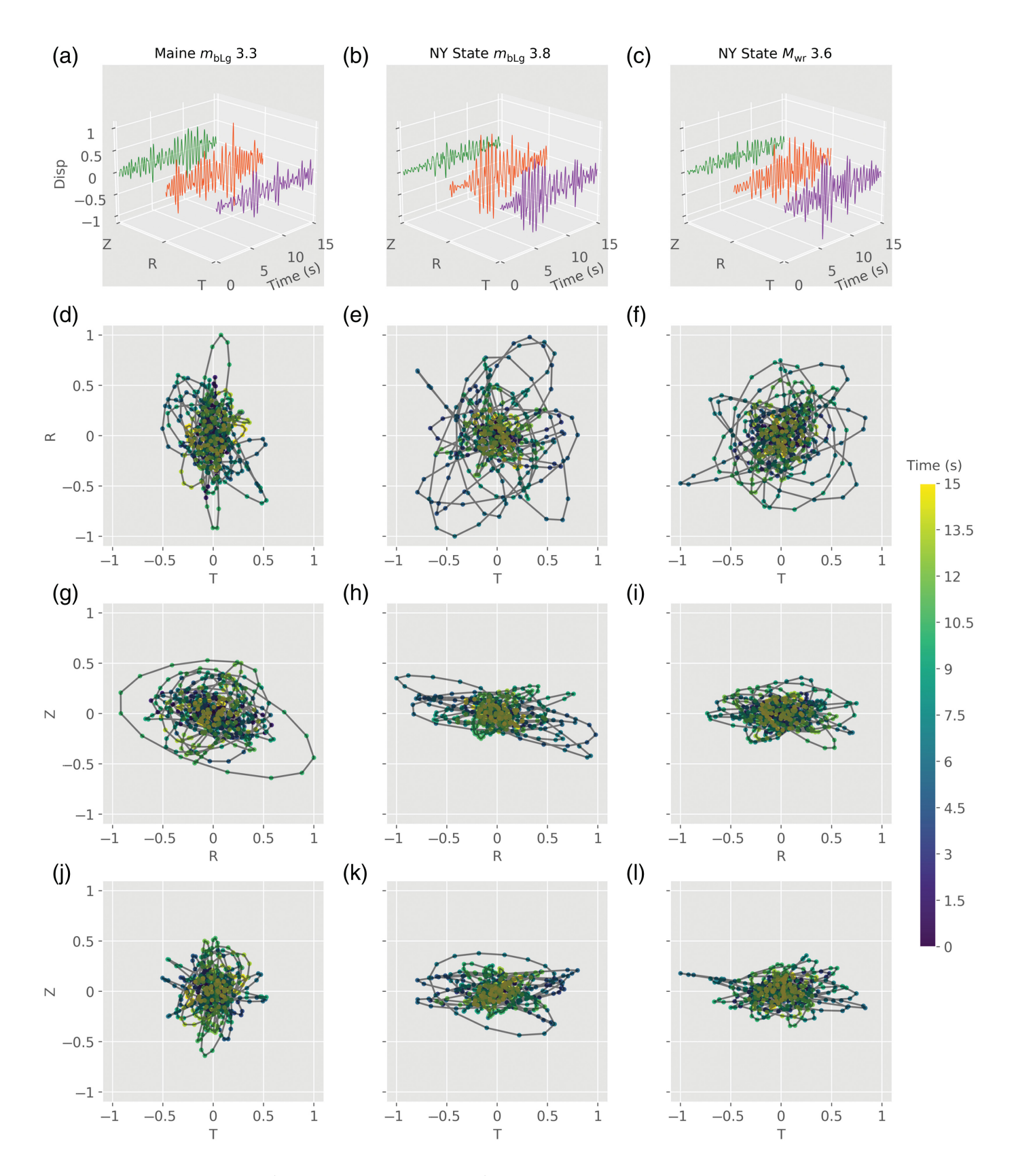


Figure 4. Zoomed phase arrivals (initial *P*-wave onset not shown) and particle motion diagrams for the *S–Lg* package of regional earthquakes in the northeastern United States (a,d,g,j: Maine $m_{\rm bLg}$ 3.3; b,e,h,k: New York $m_{\rm bLg}$ 3.8; c,f,i,l: New York $M_{\rm wr}$ 3.6). (a–c) 3D view of filtered records (1.3–4 Hz), normalized to the

absolute amplitude maximum per earthquake, and colored per component (Z: green; R: orange; and T: violet). (d–l) Particle motion showing phase polarization in (d–f) the horizontal plane and (g–i, j–l) both vertical planes, as indicated. Markers on polarization diagrams are colored according to time, as shown by scale bar at right.

subways, trains, airplanes, and helicopters), or noise generated at major public events (e.g., football matches and concerts). Any of these effects may induce ground vibrations that are visible on seismograms (e.g., Bokelmann and Baisch, 1999; Stammler and Ceranna, 2016; Díaz et al., 2017, 2022; Fuchs et al., 2018; Schippkus et al., 2020). The well-known reduction of anthropogenic noise during 2020 COVID-19 lockdowns led to a significant decrease of seismically recorded noise levels worldwide (Lecocq et al., 2020).

Exercise 5: power spectral density plots and station noise characteristics

Evaluating the noise profiles of our sensor installation requires a statistic overview of the distribution of seismic energy as a function of frequency, determined from the investigation of longer time durations, visualized as a so-called probabilistic power spectral density (PPSD) plot (e.g., McNamara and Buland, 2004; McNamara and Boaz, 2019). To estimate the PPSDs for the full range of frequencies (see Data and Resources), we avoid prefiltering or downsampling our time series during the preprocessing. Figure 5a shows PPSDs for the Z component for a selected time period. For comparison, we also show a PPSD for broadband station YLE (Fig. 5b), which was previously (unfortunately without time overlaps) installed at the same site as part of the New England Seismic Network. Station YLE recorded energy at frequencies between 0.01 and 50 Hz well, with amplitudes between the high- and low-noise-level models of Peterson (1993). It is notable that in the range typical for body-wave studies (>0.1 Hz), the Raspberry Shake performs similarly well as its broadband equivalent, although for frequencies <0.06 Hz the short-period sensor appears to reach its limits. We emphasize that PPSDs present an average distribution of energy over a long time interval of recording. In contrast, singular strong events (e.g., the Mexico earthquakes) can produce enough surface-wave energy to be detected by the Raspberry Shake, even at lower frequencies (<0.05 Hz). For higher frequencies (>1 Hz), the split of the probability density function into two distinct bands in a bimodal distribution is caused mainly by diurnal variations, due to the difference in anthropogenic noise levels between daytime (Fig. 5c) and nighttime (Fig. 5d), reflecting different levels of building use. This distinction between day and night is primarily relevant during days of the work week (Fig. 5e). The greater presence of anthropogenic noise sources during the day generally causes larger amplitudes for frequencies >1 Hz than observed during nights. Between 0.1 and 1 Hz, the daytime and nighttime distributions look similar, indicating that teleseismic earthquakes can be well recorded at all times of the day. As KGL is generally quieter on the weekends (Fig. 5f), diurnal differences in amplitudes are negligible, leading to a more unimodal distribution. On the other hand, the generally reduced noise level at weekends compared to weekly working hours explains the bimodal distribution observed during days.

A different view of the station noise characteristics is shown in Figure 6a, which displays the time series of two selected frequency bands (predefined PPSD bins) that highlight natural (2.3–4.7 s, in the microseismic band) and anthropogenic (8.8–18 Hz) noise sources. The latter clearly shows a diurnal signal, indicating daily peaks during office hours and nightly lows. Differences between a higher noise level throughout the work week and quieter weekends are also apparent. A general increase during workdays (and two Saturdays) in the middle of October is likely related to construction work, discussed subsequently.

For an Introduction to Seismology classroom exercise, we envision challenging students to generate PPSD plots in ObsPy to (1) visualize and compare noise levels at the Raspberry Shake installation with the high- and low-noise models of Peterson (1993), (2) investigate diurnal and weekly variations, and (3) identify the busiest work day in KGL over a selected period.

Exercise 6: temporal variations in the secondary microseismic peak and correlations with weather observations

In this exercise, we consider a frequency band that corresponds to a well-known local maximum in the PPSDs, the so-called secondary microseismic peak, caused by the interference of ocean waves in opposing directions, which form standing waves (e.g., McNamara and Buland, 2004; Aster et al., 2008). Because natural sources of ambient seismic noise may be affected by local or regional weather conditions (e.g., Ebeling, 2012; Sufri et al., 2014), temporal variations in our records of the secondary microseismic peak can possibly be related to weather phenomena in New England and their effects on wave heights along the Long Island Sound coastline or in the Atlantic Ocean. Analyzing Raspberry Shake records of the microseism can thus provide a fascinating entry point and motivation for students to start studying seismology, particularly in seismically quiet regions. A comparison between our microseismic noise observations (Fig. 6a; blue line: 2.3-4.7 s period band) and (Fig. 6b) oceanic-wave height records from station 44066, a buoy of the National Data Buoy Center (NDBC; see Data and Resources) in the Mid-Atlantic Bight (see e.g., Northeast Fisheries Science Center, 2024), reveal striking coincidences of both time series, suggesting that variations in the oceanic wavefield likely cause changes in recorded ambient noise. Furthermore, as local wind conditions are directly connected to the formation of waves in the Long Island Sound and nearby Atlantic, it is not surprising that firstorder trends of the microseism PPSD time series show up in wind speeds (Fig. 6c) as well. These tendencies are particularly obvious after the increase of wind speeds at the beginning of September. Although the wind intensity in general may also have an effect on our building, we do not expect direct effects to be dominant, given the relatively low building profile and the position of the sensor in the sub-basement. The increase in wind intensity was further accompanied by a change in

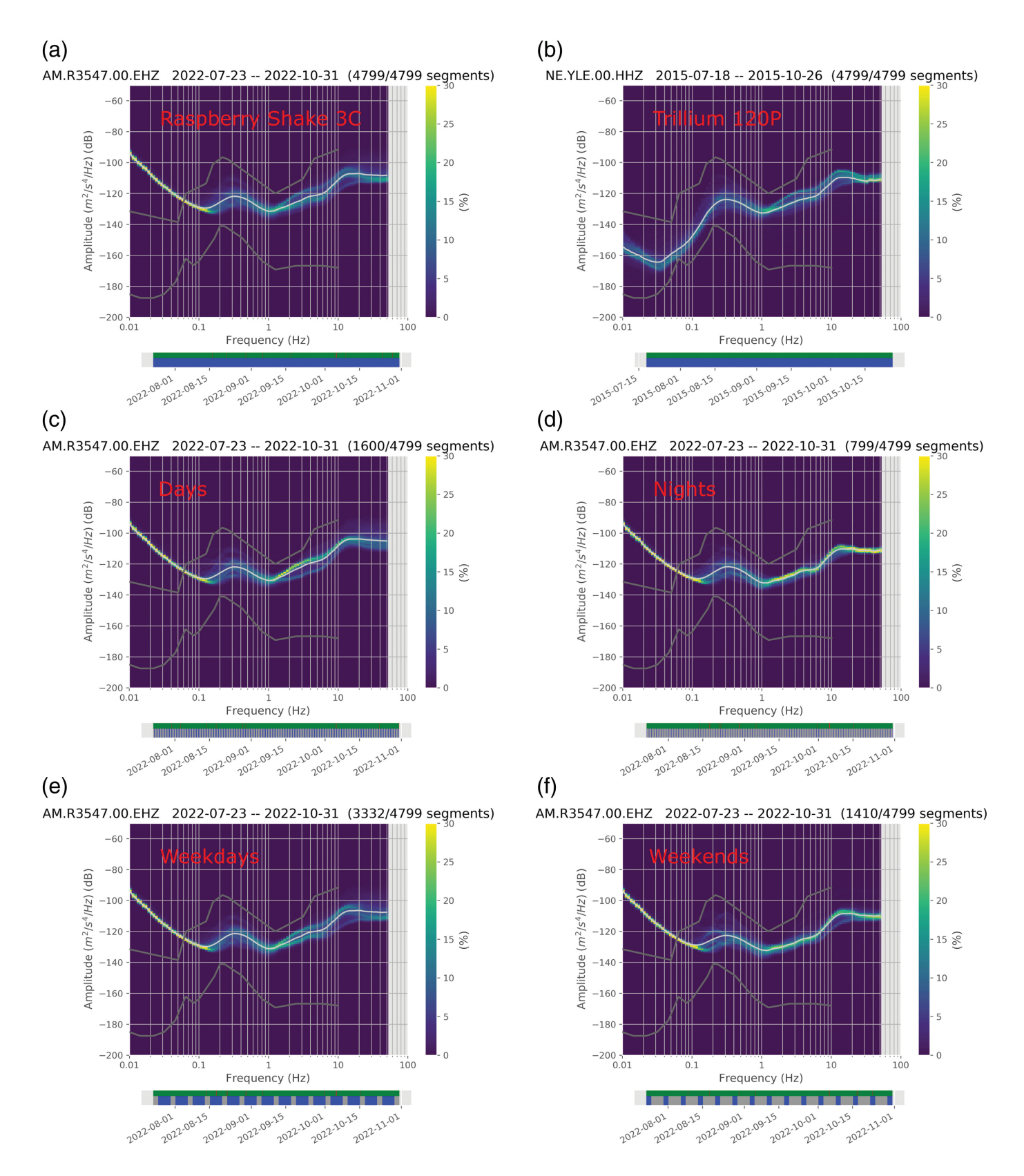
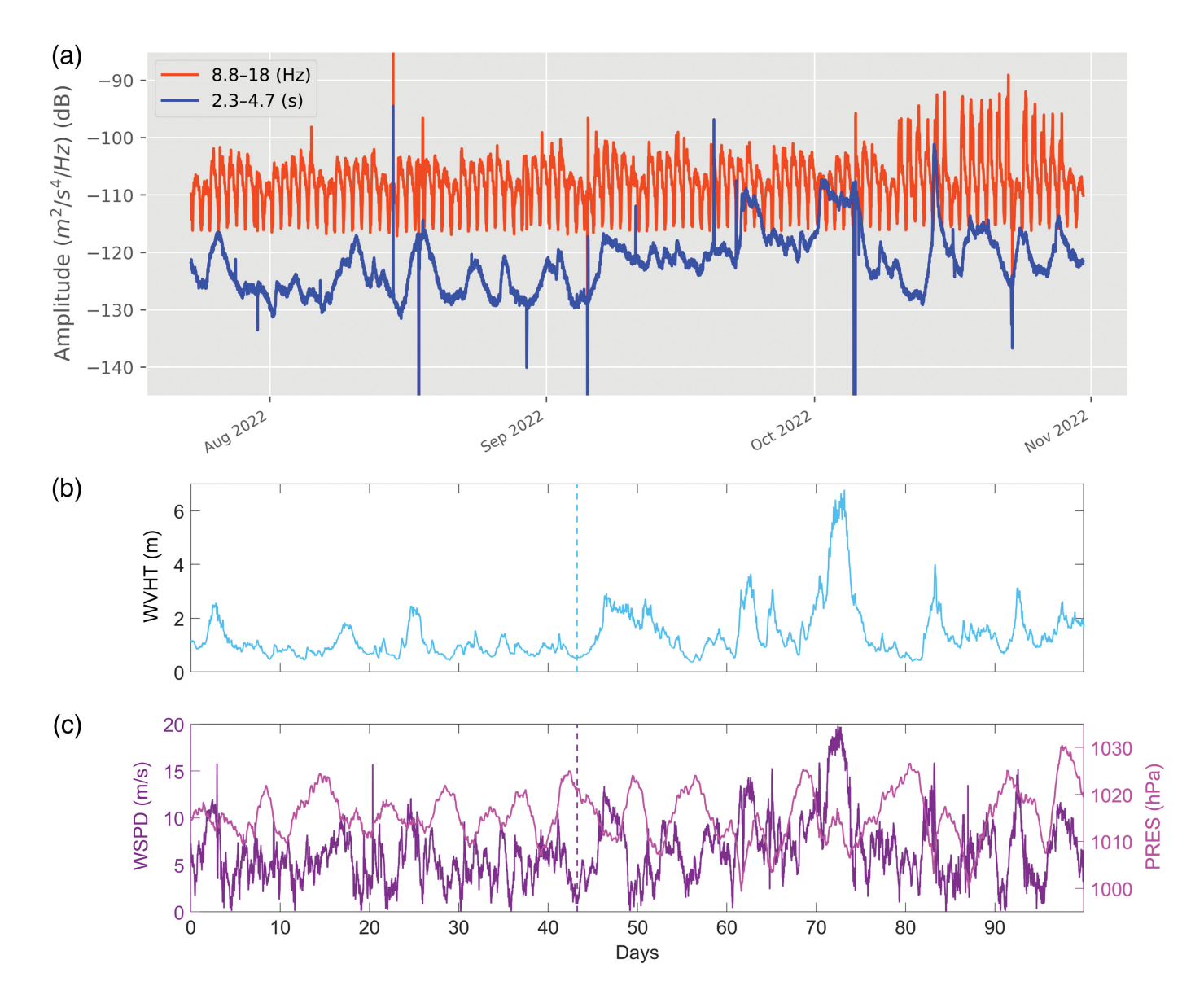


Figure 5. Probabilistic power spectral density (PPSD) plots indicating the frequency-dependent distribution of seismic energy recorded by our Raspberry Shake sensor (R3547) for selected time windows. (a) PPSD for the Z-component during 100 days of observation (July–October 2022) colored according to scale bar at right. Blue bar highlights considered time interval; green bar indicates data availability; white line shows the mean of the distribution; and gray

lines follow the high- and low-noise models of Peterson (1993). (b) PPSD for station YLE, a Trillium120P broadband sensor previously installed at the site as part of the New England Seismic Network (see Data and Resources). (c) PPSD for R3547 during (c) daytime hours, (d) nighttime hours, (e) weekdays only, and (f) weekend days only.



the dominant wind and wave direction (see supplemental exercise 6), which could explain the general increase in the level of the secondary microseismic peak at the beginning of September 2022. Given the coupling between local wind intensity and the formation of ocean waves, peaks in the microseism can potentially be indicative of passing low-pressure weather systems (Fig. 6c). For example, the remnants of hurricane Ian moved northward along the East Coast of the United States and passed by between 1 and 5 October; its presence shows up clearly as a local maximum in the ambient noise band, as a significant increase in wind speeds and comparably low to medium pressure. Similar indications can be seen for an earlier peak in microseismic noise from 22 to 24 September, tentatively associated with two phenomena: the crossing of a cold front of a low-pressure system that formed earlier over Ontario, Quebec, and the Great Lakes, and the passing and later landfall of remnants of hurricane Fiona at Nova Scotia. Another example shows up as a sharp ambient noise maximum that occurred around 14 October, which might be related

Figure 6. Noise levels recorded in KGL from anthropogenic and natural noise sources. (a) Comparison between two time series (July–November 2022) for selected frequency bands of the Raspberry Shake PPSD (Fig. 5a); orange line shows diurnal and weekly variability of anthropogenic noise (8.8–18 Hz); blue line highlights the frequency band associated with the secondary microseismic peak (2.3–4.7 s). Temporal variation of (b) wave heights (WVHT, light blue), and (c) wind speed (WSPD, violet) and atmospheric pressure (PRES, magenta) recorded at buoy 44066 of the National Data Buoy Center in the Mid-Atlantic Bight. Vertical dashed lines near the beginning of September indicate the beginning of an upward trend in WVHT, WPSD, and microseismic noise levels (associated wave and wind directions see supplement exercise 6).

to the crossing of a cold front of a stable low-pressure system that formed earlier over Manitoba.

Records from a campus-based Raspberry Shake, particularly in a setting near the coast such as Yale's campus, provide an excellent entry point for teaching about the concept of secondary microseismic peak in an introductory seismology course. We envision a classroom exercise that asks students to generate plots of noise levels in the microseismic frequency band (such as that shown in Fig. 6) and to explore temporal variations in their amplitudes. In combination with local meteorological and oceanic data from buoys, these plots can inspire students to think deeply about the physical mechanisms of microseism generation, which could then lead into discussions of classic papers on the physics of microseism (e.g., Longuet-Higgins, 1950; Hasselmann, 1963) and other well-known examples of storms causing increases in microseismic noise amplitudes (e.g., Sufri et al., 2014).

Exercise 7: anthropogenic activities and forensic seismology

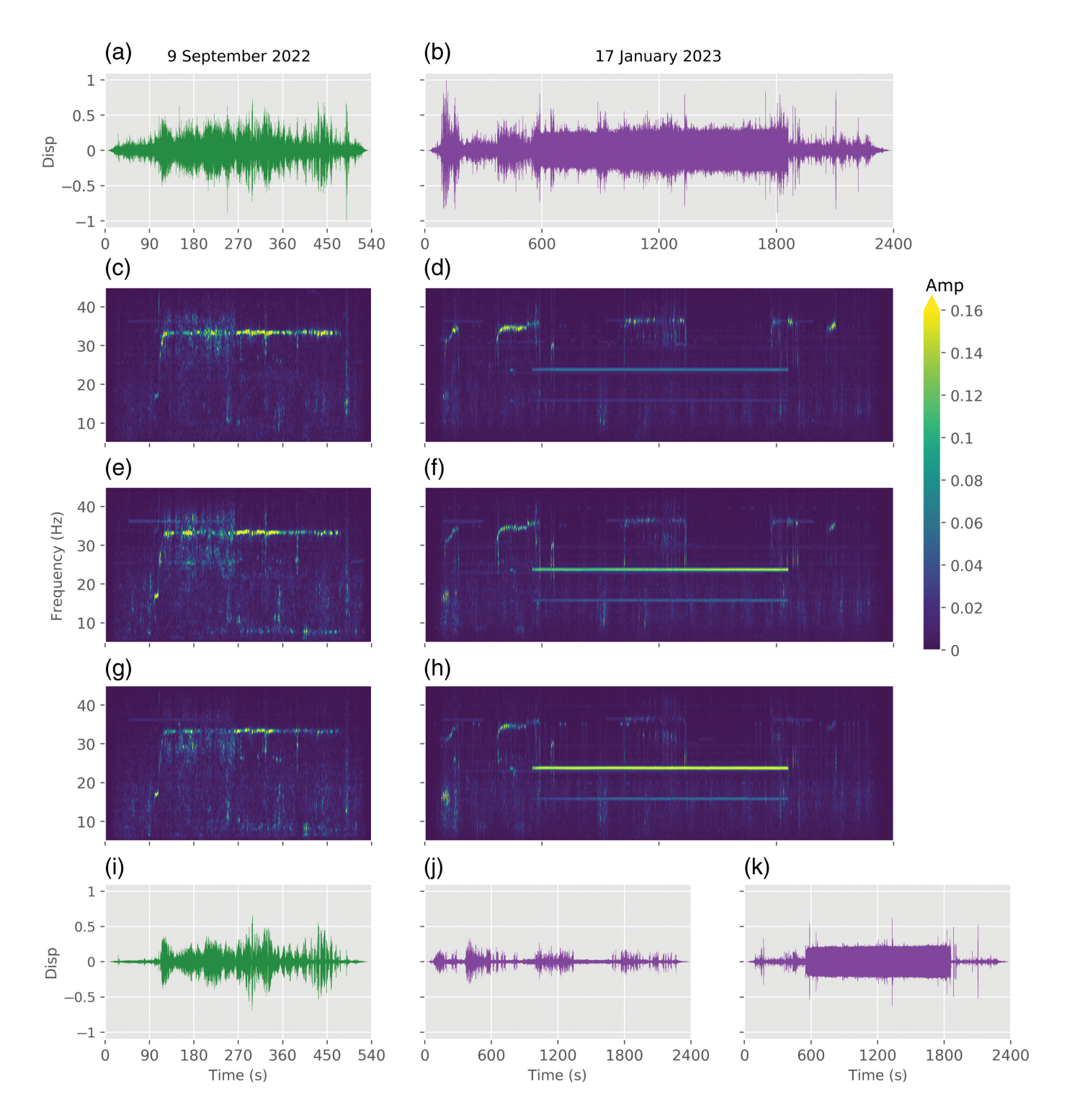
During the initial year of our Raspberry Shake deployment, a building adjacent to KGL, the Yale Peabody Museum of Natural History, was undergoing a significant renovation, with some ancillary construction work going on in KGL itself. Construction activities picked up in mid- to late October 2022, leading to the increased noise levels seen in the anthropogenic frequency band in Figure 6a. Several aspects of the construction work and its effects on our Raspberry Shake recordings lend themselves well to teaching about the use of seismology techniques to study anthropogenic phenomena (e.g., O'Hanlon, 2001). The Forensic Geoscience course at Yale, an undergraduate seminar suitable for nonscience majors, introduces the basic concepts of forensic seismology, illustrated by case studies (e.g., Kim et al., 2001; Koper et al., 2003; Mucciarelli, 2012; Dando et al., 2023). During the Fall 2023 edition of the class, examples from the Yale Raspberry Shake were used to illustrate key concepts.

To visualize signals from construction work on our seismometer, we identify days with particularly intense activity (based on levels of audible noise in KGL) and process the Raspberry Shake data to emphasize anthropogenic signals and constrain their dominant frequencies. We follow the preprocessing steps that we would apply for earthquake data, but given the different frequency range of interest, we adjust the prefilter and water level (pre_filt = [5, 6, 44, 45] Hz; water_level = 0) and omit downsampling.

In Figure 7, we show normalized time series and spectrograms [window length (wlen): 3 s; overlap percentage (per_lap): 0.985] that highlight construction-related noise sources, which led to noticeable vibrations in our KGL offices on (Fig. 7a) 9 September 2022 and (Fig. 7b) 17 January 2023. To emphasize the anthropogenic signals, we filter the records between 30 and 36 Hz for 9 September, and 22–26 Hz and 30–40 Hz for 17 January, based on indications of the dominant frequencies in their respective spectrograms (Fig. 7c,e,g and Fig. 7d,f,h). The records of 9 September (Fig. 7i) contain a signal at a constant frequency of ~33 Hz that occurred fairly continuously over a period of ~6 min. Spectral amplitudes of this signal appear

particularly strong on the Z and N component (Fig. 7c,e) but are also visible on the E component. The estimated frequency is close to that expected for a HILTI TE 1000-AVR jackhammer operated at 32.5 Hz (e.g., Hilti, 2013; McGuire, 2020). The second example, from 17 January, involves the preparation and installation of paving slabs for a new sidewalk outside of KGL. This construction work is reflected in the seismogram with two dominant signals (Fig. 7j,k) that overlap in time but are separate in the frequency domain. The shorter, repeating part starts at a similar frequency as observed for the jackhammer on 9 September and stabilizes at slightly higher frequencies, dominating on the Z component (Fig. 7d). However, the other contribution is characterized by a longer duration (~20 min) and a very consistent waveform that appears strongest on the E component (Fig. 7h) at a constant frequency of ~24 Hz, with an undertone at ~16 Hz. Based on these characteristics, we speculate that the latter contribution is related to some type of heavy machinery; however, we were unable to precisely identify the source.

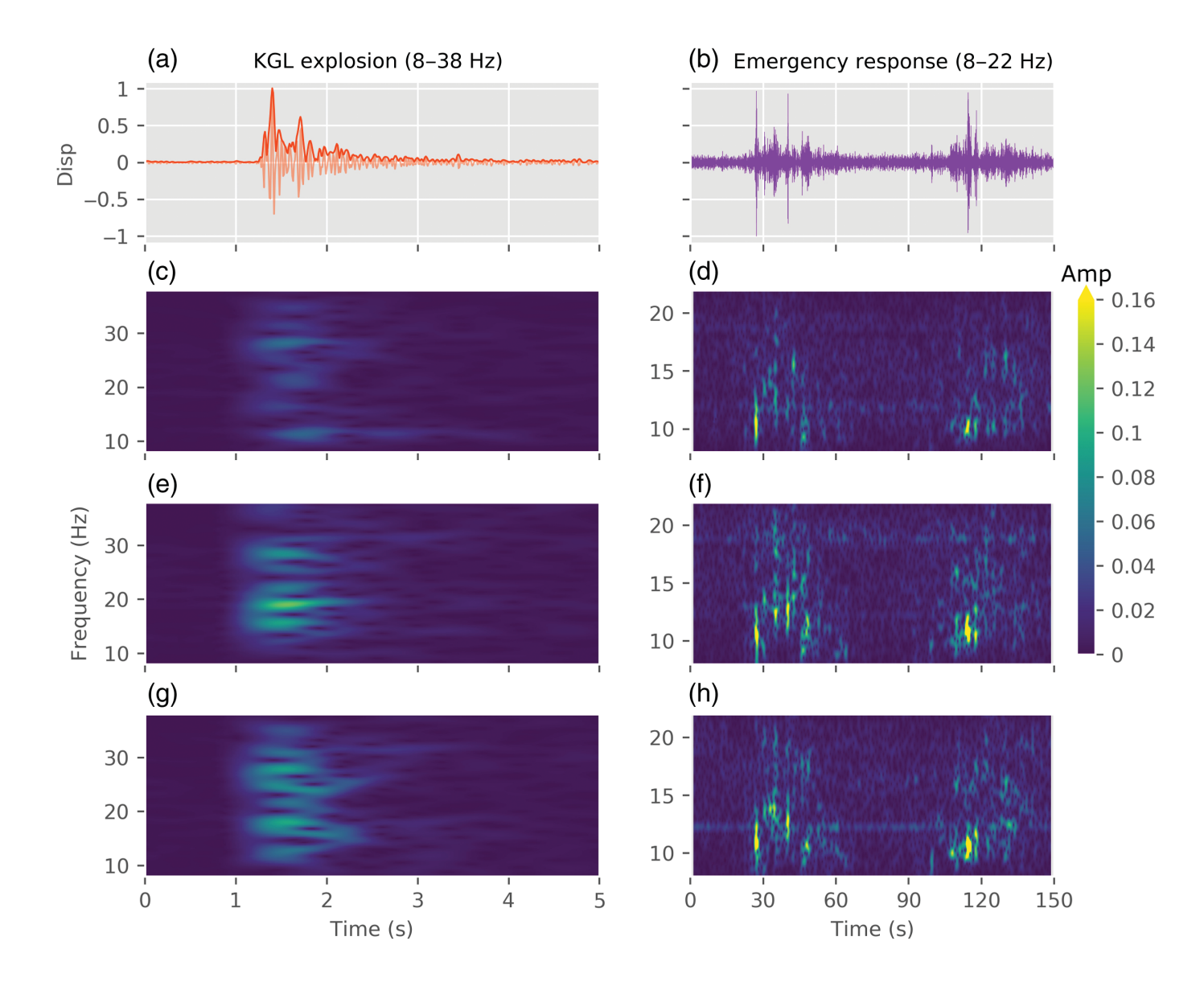
We also recorded a minor explosion in a steam tunnel related to the construction during the early morning of 27 September 2022. The detection and characterization of various explosion sources has been a common and important application of forensic seismology for a century (e.g., Wrinch and Jeffreys, 1923; Dando et al., 2023). Although the steam tunnel explosion near KGL was much less dramatic than other published examples (no injuries or significant damage), it provides a tangible and relevant case for Yale students. Figure 8 shows the preprocessed (as for Fig. 7), filtered, and normalized records of two time series and their related spectrograms [wlen $= 1.25 \text{ s (Fig. 7c,e,g)}, 3 \text{ s (Fig. 7d,f,h)}; per_lap = 0.985] from the$ early morning of 27 September 2022. Although Figure 8a indicates a clear, impulsive signal with two major peaks (highlighted by the envelope), Figure 8b shows a diffuse increase in spectral energy ~8 min later. The source of the initial signal (at t = 1-1.5 s) records the explosion (for a news report, see Sonnenfeld, 2022), which in fact was strong enough that one of the authors, at home in downtown New Haven (~1.3 km distance from KGL), was awoken by the thunderlike bang. Based on the onset of a fire alarm, Sonnenfeld (2022) reports that the explosion occurred at ~2:15 a.m. EDT. A more precise explosion time can be derived from the Raspberry Shake records. A STA/LTA analysis of the waveforms on the N component suggests the explosion happened at 2:14:56.31 a.m. EDT. In general, spectral amplitudes from this explosion appear stronger on the N- and E-component component (Fig. 8e,g). Although the distribution of spectral energy in the filtered range between 8 and 38 Hz looks comparably homogeneous on the E component, the N component indicates that two frequency bands (~15 to 19 Hz and ~29 Hz) are dominated by the acoustic waves and their interaction (coupling and wave guidance) with the structure of the building. The second signal, filtered between 8 and 22 Hz, shows two



time spans of tens of seconds with increased spectral energy that are ~50 s apart from each other. These events, which appear stronger on the horizontal components (Fig. 8f,h), are presumably related to the emergency response at the building and the arrival of the Yale Fire Marshall and the New Haven Fire Department (Sonnenfeld, 2022).

During the Forensic Geoscience classroom exercise, students will be introduced to characteristics of anthropogenic signals and learn to distinguish them from earthquakes in time- and frequency domain. To achieve the latter, they will

Figure 7. Comparison of recordings of noise from construction work for selected time periods on (left) 9 September 2022 and (right) 17 January 2023. (a,b) Unfiltered, normalized components with the strongest amplitude (Z: green; E: violet). (c–h) Related spectrograms for each component (c,d: Z; e,f: N; g,h: E) colored according to scale bar at right. (i–k) Filtered time-series components in the (i) 30–36 Hz band (for the September date), (j) 30–40 Hz band and (k) in the 22–26 Hz band (both for the January date).



create and analyze spectrograms to set up filter domains to isolate and characterize the related time series and attempt to constrain their origin (e.g., construction noise, explosion, and emergency response).

Conclusion

In this study, we have demonstrated the advantage of a low-cost, short-period Raspberry Shake sensor in a campus-based deployment for use in seismology-oriented teaching and outreach applications. We have presented examples of analyzing data recorded by a three-component (RS3D) seismograph (R3547) in ObsPy-based exercises that will support our Natural Disasters, Forensic Geoscience, and Introduction to Seismology courses at Yale. These exercises will enable upper-level seismology students to gain first hands-on experience in accessing and processing seismic data recorded on their own campus and will allow students at the introductory level to learn about concepts such as earthquakes, plate tectonics, wave propagation, ambient noise, and forensic seismology using locally recorded data examples.

Figure 8. Records of a gas explosion and subsequent emergency response at the KGL in the early morning hours of 27 September 2022. (a,b) Filtered, normalized components with the strongest amplitude (N: faded orange; E: violet), envelope (orange) highlights the "double-peak" characteristic of the explosion; (c–h) spectrograms per component (c,d: Z; e,f: N; g,h: E) colored according to the amplitude of spectral energy (scale bar at right).

Data from R3547 are also streamed to an informational screen that welcomes visitors in the KGL lobby and will be routinely incorporated in public education and outreach talks given by members of the Department of Earth and Planetary Sciences. Finally, Yale's participation in the Raspberry Shake network supports open access to seismic data and citizen science initiatives.

Data and Resources

R3547 is a part of the Raspberry Shake Network (doi: 10.7914/SN/AM), data and instrument response can be obtained via StationView

(https://stationview.raspberryshake.org/#/?lat=41.31532&lon=-72.91671 &zoom=8.000&sta=R3547). Station YLE was part of the New England Seismic Network (doi: 10.7914/SN/NE), and station information can be received via MetaData Aggregator (http://ds.iris.edu/mda/NE/YLE/? starttime=2006-12-15T00:00:00&endtime=2018-07-11T00:00:00).

Meteorological and oceanic observations of buoy station 44066 are available at the National Data Buoy Center (NDBC; https://www.ndbc. noaa.gov/station_page.php?station=44066) and can be compared with the Daily Weather Map archive (https://www.wpc.ncep.noaa.gov/ dailywxmap/). Raspberry Shake records were analyzed and visualized in JupyterLab's (https://jupyterlab.readthedocs.io/en/latest/) using ObsPy (https://docs.obspy.org/) (within Anaconda: https://anaconda. org/conda-forge/obspy), NumPy (https://numpy.org/doc/stable/user/ index.html#user), and Matplotlib (https://matplotlib.org/stable/index. html). Helpful examples to obtain and process seismic data were provided by Raspberry Shake's Developer's corner (https://manual. raspberryshake.org/developersCorner.html), the ObsPy tutorial (https:// docs.obspy.org/tutorial/), Seismo-live (http://seismo-live.org), and Computational Seismology (https://computational-seismology.github. io/learn-seismic-tomography/building-blocks/pre-processing/). For further information on the implementation of deconvolution, filter, and probabilistic power spectral density (PPSD) settings see the related ObsPy tutorials on Trace.remove_response (https://docs.obspy.org/ packages/autogen/obspy.core.trace. Trace.remove_response.html, last accessed April 2024), Stream.filter (https://docs.obspy.org/packages/ autogen/obspy.core.stream. Stream.filter.html; band-pass options: https://docs.obspy.org/packages/autogen/obspy.signal.filter.bandpass. html#obspy.signal.filter.bandpass), and PPSD determination (https:// docs.obspy.org/packages/autogen/obspy.signal.spectral_estimation. PPSD.html; https://docs.obspy.org/tutorial/code_snippets/probabilistic_ power_spectral_density.html; histogram options: https://docs.obspy. org/packages/autogen/obspy.signal.spectral_estimation.PPSD.calculate_ histogram.html#obspy.signal.spectral_estimation.PPSD.calculate_ histogram). MATLAB (https://www.mathworks.com/help/matlab/) was used to visualize the buoy time series. Figure 2 was created with the Generic Mapping Tools (GMT) (http://gmt.soest.hawaii.edu/doc/5.4.3/ gmt.html) using ETOPO1 (https://www.ncei.noaa.gov/access/metadata/ landing-page/bin/iso?id=gov.noaa.ngdc.mgg.dem:316) of Amante and Eakins (2009) and digital elevation model (DEM) segments from Digital Data (http://www.viewfinderpanoramas.org/Coverage% 20map%20viewfinderpanoramas_org3.htm) as basemaps. The GMT version of the plate boundaries of Bird (2003) has been provided PaleoEarthLabs (https://wiki.paleoearthlabs.org/doku.php?id= scientificdata:platetectonics:birdplateboundaries). Slab2.0-depth contours of Hayes et al. (2018) are available at ScienceBase-Catalog (doi: 10.5066/F7PV6JNV; Central America: https://www.sciencebase.gov/ catalog/item/5aa31127e4b0b1c392ea3e68). Focal mechanisms are based on the Global Centroid Moment Tensor (Global CMT) catalog (https:// www.globalcmt.org/CMTsearch.html) following Dziewonski et al. (1981) and Ekström et al. (2012). The Global CMT catalog and all other listed databases were last accessed in September 2023 and NDBC website was last accessed in January 2024. The supplemental material contains the full details of the methodology of exercises 2 and 3. Furthermore, it includes complementary subsections to exercise 2 on "Defining a filter range" and "Resolving low frequencies with a Raspberry Shake," and provides additional information on wind and wave directions for exercise 6.

Declaration of Competing Interests

The authors acknowledge that there are no conflicts of interest recorded.

Acknowledgments

The authors thank the ObsPy Development Team that implemented and documented the functions that lay the foundation for the exercises developed in this article, the Python community for their helpful thoughts on using NumPy and Matplotlib libraries, and Daniel Pereira for making the MATLAB Wind Rose toolbox publicly available. The authors acknowledge Raspberry Shake for hosting and maintaining an open-access network that fosters seismic data exchange between the public and research seismologists, David Rossman for his IT support during the installation of the sensor and the implementation of the livestream on the Kline Geology Laboratory's (KGL) informational screens, and Will Frazer for his assistance with the installation. The authors thank Richard Boardman of the Yale Peabody Museum for facilitating access to the KGL sub-basement. Finally, the authors thank Alan Kafka and an anonymous reviewer for constructive comments that helped them to improve the article. This work was funded by the National Science Foundation (NSF, Award Number: EAR-2153688).

References

- Amante, C., and B. W. Eakins (2009). ETOPO1 1 Arc-minute global relief model: Procedures, data sources and analysis, NOAA Technical Memorandum NESDIS NGDC-24, National Geophysical Data Center, NOAA, doi: 10.7289/V5C8276M.
- Aster, R. C., D. E. McNamara, and P. D. Bromirski (2008). Multidecadal climate-induced variability in microseisms, *Seismol. Res. Lett.* **79**, no. 2, 194–202, doi: 10.1785/gssrl.79.2.194.
- Beyreuther, M., R. Barsch, L. Krischer, T. Megies, Y. Behr, and J. Wassermann (2010). ObsPy: A python toolbox for seismology, *Seismol. Res. Lett.* **81,** no. 3, 530–533, doi: 10.1785/gssrl.81.3.530.
- Bird, P. (2003). An updated digital model of plate boundaries, *Geochem. Geophys. Geosys.* **4**, no. 3, 1–52, doi: 10.1029/2001GC000252.
- Bokelmann, G. H. R., and S. Baisch (1999). Nature of Narrow-Band Signals at 2.083 Hz, *Bull. Seismol. Soc. Am.* **89**, no. 1, 156–164, doi: 10.1785/bssa0890010156.
- Bormann, P., K. Klinge, and S. Wendt (2014). Data analysis and seismogram interpretation, in *New Manual of Seismological Observatory Practice 2 (NMSOP-2)*, P. Bormann (Editor), Deutsches GeoForschungsZentrum GFZ, Potsdam, Germany, 1–126, doi: 10.2312/GFZ.NMSOP-2_ch11.
- Calais, E., D. Boisson, S. Symithe, R. Momplaisir, C. Prépetit, S. Ulysse, G. P. Etienne, F. Courboulex, A. Deschamps, T. Monfret, et al. (2019). Can a raspberry shake seismic network complement a national seismic network? A case study in Haiti, Eos 100, 1–5, doi: 10.1029/2019EO123345.
- Dando, B. D. E., B. P. Goertz-Allmann, Q. Brissaud, A. Köhler, J. Schweitzer, T. Kværna, and A. Liashchuk (2023). Identifying attacks in the Russia Ukraine conflict using seismic array data, *Nature* doi: 10.1038/s41586-023-06416-7.
- Díaz, J., I. DeFelipe, M. Ruiz, J. Andrés, P. Ayarza, and R. Carbonell (2022). Identification of natural and anthropogenic signals in controlled source seismic experiments, *Sci. Rep.* **12**, no. 3171, 1–14, doi: 10.1038/s41598-022-07028-3.

- Díaz, J., M. Ruiz, P. S. Sánchez-Pastor, and P. Romero (2017). Urban Seismology: On the origin of earth vibrations within a city, *Sci. Rep.* 7, no. 15296, 1–11, doi: 10.1038/s41598-017-15499-y.
- Diaz, J., M. Schimmel, M. Ruiz, and R. Carbonell (2020). Seismometers within cities: A tool to connect earth sciences and society, *Front. Earth Sci.* **8**, no. 9, 1–7, doi: 10.3389/feart.2020.00009.
- Dziewonski, A. M., T. A. Chou, and J. H. Woodhouse (1981). Determination of earthquake source parameters from waveform data for studies of global and regional seismicity, *J. Geophys. Res.* **86,** no. B4, 2825–2852, doi: 10.1029/JB086iB04p02825.
- Ebeling, C. W. (2012). Inferring Ocean storm characteristics from ambient seismic Noise. A historical perspective, in *Advances in Geophysics*, R. Dmowska (Editor), Vol. 53, Elsevier, Amsterdam, Netherlands, 1–33, doi: 10.1016/B978-0-12-380938-4.00001-X.
- Ekström, G. (2014). Love and Rayleigh phase-velocity maps, 5-40 s, of the western and central USA from USArray data, *Earth Planet. Sci. Lett.* **402**, 42–49, doi: 10.1016/j.epsl.2013.11.022.
- Ekström, G., M. Nettles, and A. M. Dziewoński (2012). The global CMT project 2004-2010: Centroid-moment tensors for 13,017 earthquakes, *Phys. Earth Planet. In.* **200/201**, 1–9, doi: 10.1016/j.pepi.2012.04.002.
- Fuchs, F., G. Bokelmann, and , and AlpArray Working Group (2018). Equidistant spectral lines in train vibrations, *Seismol. Res. Lett.* 89, no. 1, 56–66, doi: 10.1785/0220170092.
- Hanna, J., and M. D. Long (2012). SKS splitting beneath Alaska: Regional variability and implications for subduction processes at a slab edge, *Tectonophysics* **530/531**, 272–285, doi: 10.1016/j.tecto.2012.01.003.
- Hasselmann, K. (1963). A statistical analysis of the generation of microseisms, *Rev. Geophys.* 1, no. 2, 177–210, doi: 10.1029/ RG001i002p00177.
- Hayes, G. P., G. L. Moore, D. E. Portner, M. Hearne, H. Flamme, M. Furtney, and G. M. Smoczyk (2018). Slab2, a comprehensive subduction zone geometry model, *Science* 362, no. 6410, 58–61, doi: 10.1126/science.aat4723.
- Hilti (2013). Hilti, *TE 1000-AVR/TE 1500-AVR*, available at https://manualzz.com/doc/5297550/te-1000-avr---te-1500-avr (last accessed August 2023).
- Kennett, B. L. N., and E. R. Engdahl (1991). Traveltimes for global earthquake location and phase identification, *Geophys. J. Int.* **105**, no. 2, 429–465, doi: 10.1111/j.1365-246X.1991.tb06724.x.
- Kim, W. Y., L. R. Sykes, J. H. Armitage, J. K. Xie, K. H. Jacob, P. G. Richards, M. West, F. Waldhauser, J. Armbruster, L. Seeber, et al. (2001). Seismic waves generated by aircraft impacts and building collapses at world trade center, New York city, Eos Trans. AGU 82, no. 47, 565–571, doi: 10.1029/01EO00330.
- Koper, K. D., T. C. Wallace, and R. C. Aster (2003). Seismic recordings of the Carlsbad, New Mexico, pipeline explosion of 19 August 2000, *Bull. Seismol. Soc. Am.* 93, no. 4, 1427–1432, doi: 10.1785/0120020192.
- Krischer, L., T. Megies, R. Barsch, M. Beyreuther, T. Lecocq, C. Caudron, and J. Wassermann (2015). ObsPy: A bridge for seismology into the scientific Python ecosystem, *Comput. Sci. Discov.* 8, no. 1, 1–17, doi: 10.1088/1749-4699/8/1/014003.
- Lamb, O. D., M. J. Shore, J. M. Lees, S. J. Lee, and S. M. Hensman (2021). Assessing Raspberry Shake and Boom Sensors for recording African elephant acoustic vocalizations, *Front. Conserv. Sci.* 1, doi: 10.3389/fcosc.2020.630967.

- Lecocq, T., S. P. Hicks, K. V. Noten, K. V. Wijk, and P. Koelemeijer (2020). Global quieting of high-frequency seismic noise due to COVID-19 pandemic lockdown measures, *Science* **369**, no. 6509, 1338–1343, doi: 10.1126/science.abd2438.
- Longuet-Higgins, M. S. (1950). A theory of the origin of microseisms, *Phil. Trans. Roy. Soc. Lond. A* **243**, no. 857, 1–35, doi: 10.1098/rsta.1950.0012.
- Lynner, C., H. J. A. Van Avendonk, A. Bécel, G. L. Christeson, B. Dugan, J. B. Gaherty, S. Harder, M. J. Hornbach, D. Lizarralde, M. D. Long, et al. (2019). The eastern North American margin community seismic experiment: An amphibious active- and passive-source dataset, Seismol. Res. Lett. 91, no. 1, 533–540, doi: 10.1785/0220190142.
- Manconi, A., V. Coviello, M. Galletti, and R. Seifert (2018). Short communication: Monitoring rockfalls with the Raspberry Shake, *Earth Surf. Dynam.* 6, no. 4, 1219–1227, doi: 10.5194/esurf-6-1219-2018.
- McGuire, S. (2020). Design and testing of a high frequency hydraulic mechanical jackhammer, *Master Thesis*, available at https://escholarship.mcgill.ca/concern/theses/0c483q02p (last accessed August 2023).
- McNamara, D. E., and R. I. Boaz (2019). Visualization of the seismic ambient noise spectrum, in *Seismic Ambient Noise*, N. Nakata, L. Gualtieri, and A. Fichtner (Editors), Cambridge University Press, Cambridge, United Kingdom, 1–29, doi: 10.1017/9781108264808.003.
- McNamara, D. E., and R. P. Buland (2004). Ambient noise levels in the continental United States, *Bull. Seismol. Soc. Am.* **94**, no. 4, 1517–1527, doi: 10.1785/012003001.
- Megies, T., M. Beyreuther, R. Barsch, L. Krischer, and J. Wassermann (2011). ObsPy what can it do for data centers and observatories? *Ann. Geophys.* **54**, no. 1, 47–58, doi: 10.4401/ag-4838.
- Mucciarelli, M. (2012). The seismic wake of Costa Concordia, *Seismol. Res. Lett.* **83**, no. 4, 636–638, doi: 10.1785/0220120020.
- Northeast Fisheries Science Center (2024). Ecology of the Northeast US Continental Shelf: Physical setting and habitat, available at https://apps-nefsc.fisheries.noaa.gov/nefsc/ecosystem-ecology/physical.html (last accessed January 2024).
- O'Hanlon, L. (2001). Seismic sleuths. *Nature* **411**, 734–736, doi: 10.1038/35081281.
- Peterson, J. (1993). Observations and modeling of seismic background noise, *Technical Report*, doi: 10.3133/ofr93322.
- Raspberry Shake (2018). How does the Raspberry Shake compare to a broadband seismometer? available at https://manual.raspberryshake .org/bru2.html#bru2comparison (last accessed April 2024).
- Raspberry Shake (2020). Raspberry shake technical specifications specifications for: raspberry shake 3D, availabl at https://manual.raspberryshake.org/_downloads/RSGlobalTechnicalSpecifications Document.pdf (last accessed April 2024).
- Raspberry Shake (2023). Raspberry Shake Publications & Case Studies, available at https://raspberryshake.org/news/scientific-posters/ (last accessed April 2024).
- Reiss, M. C., M. D. Long, and N. Creasy (2019). Lowermost mantle anisotropy beneath Africa from differential SKS-SKKS shear-wave splitting, J. Geophys. Res. 124, no. 8, 8540–8564, doi: 10.1029/ 2018JB017160.
- Schippkus, S., M. Garden, and G. Bokelmann (2020). Characteristics of the ambient seismic field on a large-N seismic array in the

- Vienna Basin, Seismol. Res. Lett. **91,** no. 5, 2803–2816, doi: 10.1785/0220200153.
- Sonnenfeld, S. (2022). Steam explosion at Peabody Museum traced to pipe leak, *Yale Daily News*, CXLV, available at https://yaledailynews.com/blog/2022/09/28/steam-explosion-at-peabody-museum-traced-to-pipe-leak/ (last accessed September 2023).
- Stammler, K., and L. Ceranna (2016). Influence of wind turbines on seismic records of the Gräfenberg array, *Seismol. Res. Lett.* **87**, no. 5, 1075–1081, doi: 10.1785/0220160049.
- Subedi, S., G. Hetényi, P. Denton, and A. Sauron (2020). Seismology at school in Nepal: A program for educational and citizen seismology through a low-cost seismic network, *Front. Earth Sci.* **8**, no. 73, 1–19, doi: 10.3389/feart.2020.00073.
- Sufri, O., K. D. Koper, R. Burlacu, and B. de Foy (2014). Microseisms from Superstorm Sandy, *Earth Planet. Sci. Lett.* **402**, 324–336, doi: 10.1016/j.epsl.2013.10.015.
- Winter, K., D. Lombardi, A. Diaz-Moreno, and R. Bainbridge (2021). Monitoring icequakes in east antarctica with the raspberry

- shake, Seismol. Res. Lett. **92**, no. 5, 2736–2747, doi: 10.1785/0220200483.
- Wrinch, D., and H. Jeffreys (1923). On the seismic waves from the Oppau explosion of 1921 Sept. 21, *Geophys. J. Int.* 1, no. S2, 15–22, doi: 10.1111/j.1365-246X.1923.tb06565.x.
- Zenhäusern, G., S. C. Stähler, J. F. Clinton, D. Giardini, S. Ceylan, and R. F. Garcia (2022). Low-frequency marsquakes and where to find them: Back azimuth determination using a polarization analysis approach, *Bull. Seismol. Soc. Am.* 112, no. 4, 1787–1805, doi: 10.1785/0120220019.
- Zhao, L. F., and S. M. Mousavi (2018). Lateral variation of crustal Lg attenuation in Eastern North America, *Sci. Rep.* **8**, no. 7285, 1–16, doi: 10.1038/s41598-018-25649-5.

Manuscript received 31 October 2023 Published online 28 May 2024